PHOTONICS Research

Intermodal four-wave mixing in silicon waveguides

Stefano Signorini,[1,*] Mattia Mancinelli,[1,2] Massimo Borghi,[1] Martino Bernard,[3] Mher Ghulinyan,[4] Georg Pucker,[4] and Lorenzo Pavesi[1]

[1]Department of Physics, University of Trento, Via Sommarive 14, 38123 Trento, Italy
[2]SM Optics s.r.l., Research Programs, Via John Fitzgerald Kennedy 2, 20871 Vimercate, Italy
[3]Department of Information Engineering, University of Brescia, Via Branze 38, 25123 Brescia, Italy
[4]Centre for Materials and Microsystems, Fondazione Bruno Kessler, 38123 Trento, Italy
*Corresponding author: stefano.signorini-1@unitn.it

Received 6 February 2018; revised 9 May 2018; accepted 10 May 2018; posted 15 May 2018 (Doc. ID 319640); published 20 July 2018

In this work, we report the modeling and the experimental demonstration of intermodal spontaneous as well as stimulated four-wave mixing (FWM) in silicon waveguides. In intermodal FWM, the phase-matching condition is achieved by exploiting the different dispersion profiles of the optical modes in a multimode waveguide. Since both the energy and the wave vectors have to be conserved in the FWM process, this leads to a wide tunability of the generated photon wavelength, allowing us to achieve a large spectral conversion. We measured several waveguides that differ by their widths and demonstrate large signal generation spanning from the pump wavelength (1550 nm) down to 1202 nm. A suited setup evidences that the different waves propagated indeed on different order modes, which supports the modeling. Despite observing a reduced efficiency with respect to intramodal FWM due to the decreased modal overlap, we were able to show a maximum spectral distance between the signal and idler of 979.6 nm with a 1550 nm pump. Our measurements suggest the intermodal FWM is a viable means for large wavelength conversion and heralded photon sources.

OCIS codes: (190.4380) Nonlinear optics, four-wave mixing; (130.7405) Wavelength conversion devices; (230.7380) Waveguides, channeled.

https://doi.org/10.1364/PRJ.6.000805

1. INTRODUCTION

Wavelength division multiplexing (WDM) is a well-established approach to high-capacity data transfer [1]. The efficiency of WDM could be further improved by using mode division multiplexing (MDM), where multimode optical fibers or waveguides are used [2,3]. The combination of WDM and MDM could be the next step in the evolution of optical communication technology [4]. While WDM has been extensively studied and optimized, MDM is currently under development. Among the most useful functionalities, there is mode-selective wavelength conversion for high-speed and controllable on-chip data transfer [5–7]. This is a nonlinear optical technique that is based on four-wave mixing (FWM) [8]. FWM is a third-order nonlinear optical process involving four optical waves in a medium. In spontaneous FWM (SFWM), two waves at the input, called the pumps, mix up to generate two new optical waves called the signal and the idler. When a seed optical wave is input together with the two pump waves, the process is named stimulated FWM (sFWM), and the seed wave is converted into the new generated wave: in this way wavelength conversion is achieved [9]. For mode-selective wavelength conversion in silicon-on-insulator (SOI) waveguides, sFWM has been used in its degenerate version, where the two pump waves have the same wavelength [5,7]. Intramodal FWM, i.e., with all the waves on the same optical mode, has been extensively studied in the last 50 years [8]. On the contrary, intermodal FWM, i.e., with the signal, the idler, and the pump on different modes, has never been studied in a waveguide. Intermodal FWM has the advantage of not requiring anomalous group velocity dispersion (GVD), which is usually considered for intramodal FWM to achieve phase matching [10,11]. This results in an easier handling of the phase-matching condition [12]. The intermodal FWM exhibits higher flexibility, larger spectral conversion, and easier phase matching [13–18]. Up to now, intermodal FWM has been demonstrated only in higher-order-mode optical fibers [12,19,20] and in photonic crystal optical fibers [21].

Here, we demonstrate on-chip intermodal FWM, both for SFWM and sFWM, extending our preliminary work [22]. We investigate extensively a particular modal combination

involving the pump on both the first and second transverse-electric (TE) modes and the signal and idler on, respectively, the second and first TE modes. Moreover, we also report other modal combinations, involving up to the third-order mode and with both TE and transverse-magnetic (TM) polarization. By engineering the waveguide geometry, we control the modal dispersions, and we achieve the phase-matching condition. An example of on-chip intermodal phase matching has been reported very recently with Brillouin scattering in silicon waveguides [23]. What is interesting in intermodal phase matching is the fact that, depending on the excited optical modes and on the geometry of the waveguide, the wavelength of the phase-matched discrete bands can be easily controlled. We demonstrate that this allows getting large spectral conversion. In fact, we show SFWM with an idler at a wavelength of 1202 nm when the pump is at 1550 nm. To the best of our knowledge, this is the largest spectral detuning achieved by FWM in an SOI waveguide with a C-band pump. This paves the way for the application of intermodal FWM for broadband and highly tunable on-chip wavelength conversion, such as in gas sensing [24], mid-infrared (MIR) detection [25], and MIR light generation [26]. Moreover, the large detuning combined with the spontaneous generation can be used to get an on-chip heralded single-photon source with the heralded photon generated at short wavelengths, where highly efficient single-photon detectors are available, and the heralded photon generated beyond 2 μm. This can be of great interest for free-space quantum communications [27].

The paper is organized as follows. In Section 2 we describe the theory of intermodal FWM and of mode coupling. In Section 3 we detail the setup used and the measurements, and we discuss the obtained results. Section 4 summarizes the main results and reports on the perspectives.

2. THEORY

A. Multimode Waveguides

The typical cross section of our waveguides is reported in Fig. 1(a). On an SOI 6' wafer, with a buried oxide layer (BOX) of 3 μm and a silicon device layer of 243 nm, waveguides were defined by 365 nm lithography. Reactive ion etching was used to pattern the waveguides, which were then cladded by 900 nm thick SiO_2 deposited by plasma-enhanced chemical vapor deposition (PECVD). The waveguide width ranged from 2 to 3.8 μm.

By using a commercial finite element method (FEM) software (COMSOL), we computed the modal field profiles and the effective indices for these multimode waveguides. As an example, the profiles and the effective index dispersions are reported in Fig. 1(b) and Figs. 1(c) and 1(d), respectively, for various waveguide widths. In particular, Figs. 1(c) and 1(d) show that we can control the effective index value of the propagating optical mode by selective excitation of a specific optical mode at a given wavelength. Moreover, the index dispersion also depends critically on the waveguide width, as reported in Figs. 1(c) and 1(d). Tailoring the index dispersion through the geometry of the waveguide is of crucial importance for the control of the phase-matching condition [28].

B. Intermodal Four-Wave Mixing

In the degenerate FWM, the two pumps have the same frequency ω_P, and the signal and the idler have frequencies ω_S and ω_I, with $\omega_S < \omega_I$ by convention. Despite the two pumps having the same frequency, in a multimode waveguide they can propagate on different waveguide modes, thus with different effective indices n_{eff}. Since the wave vector is written as $k = \frac{\omega}{c} n_{\text{eff}}$, with c the light velocity, the result is that the two pumps have the same frequency but with different wave vectors.

Both spontaneous FWM as well as stimulated FWM are ruled by the energy conservation relation from Eq. (1) and the momentum conservation relation from Eq. (2)

$$\omega_P + \omega_P = \omega_S + \omega_I, \tag{1}$$

$$k_{P1} + k_{P2} = k_S + k_I, \tag{2}$$

where the subscripts $P1$, $P2$, S, I refer to the first pump, second pump, signal, and idler, respectively.

Provided that Eq. (1) is fulfilled, the efficiency η of SFWM and sFWM scales with the phase mismatch Δk as [9]

$$\eta \propto |f_{jqlm}|^2 \,\text{sinc}\left(\Delta k \frac{L}{2\pi}\right)^2, \tag{3}$$

where L is the nonlinear medium length, f_{jqlm} is the mode field overlap, with j, q, l, m indicating, respectively, the mode orders for the two pump photons, the signal, and the idler photons. The phase mismatch Δk is given by

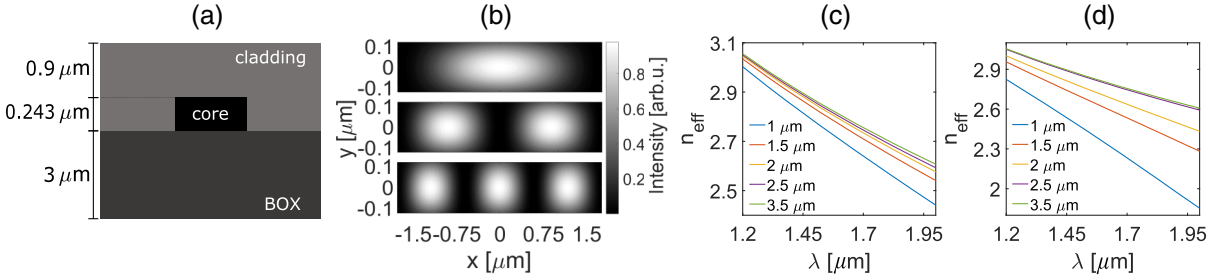

Fig. 1. (a) Cross section of the waveguides used in this work. BOX refers to the buried oxide. The core is made of crystalline Si, and the cladding by deposited SiO_2. (b) Computed intensity profiles in the core region of the first three TE modes supported by a 3.5-μm-wide waveguide. (c) Effective index as a function of the wavelength for the first TE mode for the different waveguide widths reported in the legend. (d) Effective index as a function of the wavelength for the second TE mode for the different waveguide widths reported in the legend.

$$\Delta k = \Delta k_L + \Delta k_{NL}, \tag{4}$$

where $\Delta k_L = k_S + k_I - k_{P1} - k_{P2}$ is the linear phase mismatch and $\Delta k_{NL} = \gamma_{P1} P_{P1} + \gamma_{P2} P_{P2}$ quantifies the phase contribution to Δk due to the self-phase modulation (SPM) of the pumps [14]. γ_{P1} and γ_{P2} are the nonlinear coefficients for the two pumps [9], and P_{P1}, P_{P2} are the powers of the two pumps.

In a multimode waveguide, the dispersion of the higher-order modes can be used to tune the spectral position of the FWM phase-matching condition [29]. Δk_L in a multimode waveguide can be written as [30]

$$\Delta k_L = \frac{\omega_P}{c} n_{\text{eff}}^{j}(\omega_P) + \frac{\omega_P}{c} n_{\text{eff}}^{q}(\omega_P) - \frac{\omega_S}{c} n_{\text{eff}}^{l}(\omega_S) - \frac{\omega_I}{c} n_{\text{eff}}^{m}(\omega_I), \tag{5}$$

where j, q, l, m are as in Eq. (3). In the following we use the convention that the modal combination involved in the FWM process is indicated as (j, q, l, m), i.e., one pump photon on the jth order mode, the other pump photon on the qth order mode, the signal photon on the lth order mode, and the idler on the mth order mode.

By computing the effective index for the different modes and by using Eqs. (4) and (5), we found that the combination (1,2,2,1) with all the modes with a TE polarization is the best candidate to validate the intermodal FWM, in both the spontaneous and stimulated cases.

Figure 2 compares the spectral dependence of the idler generation efficiency from Eq. (3) for the intramodal and intermodal degenerate FWM with pump photons at 1550 nm. If the waves involved in the process propagate on the same first-order mode, the maximum efficiency is only close to the pump wavelength. When the intermodal combination is excited, the spectral position of the phase matching is moved far from the pump wavelength, allowing for large wavelength conversion. This figure shows the potential of the intermodal FWM.

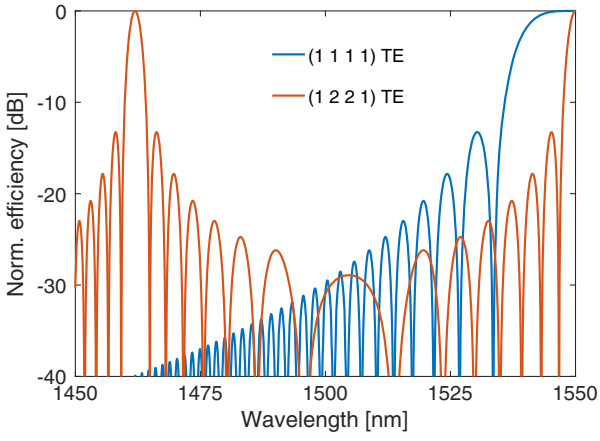

Fig. 2. Spectral dependence of the idler generation efficiency for the (1,1,1,1) intramodal FWM and for the (1,2,2,1) intermodal FWM. All waves have TE polarization. A silicon waveguide with a cross section 3.5 μm × 243 nm was assumed in the calculation. Each efficiency is normalized to its maximum.

As shown by Eq. (3), the efficiency of FWM scales quadratically with the modulus of the mode fields overlap f_{jqlm} and f_{jqlm} for the intermodal combination (j, q, l, m), assuming all the waves have the same polarization, is given by [14]

$$f_{jqlm} = \frac{\int_{A_0} E_j(r,\omega_j) E_q(r,\omega_q) E_l^*(r,\omega_l) E_m^*(r,\omega_m) A}{\prod_{i=jqlm} \left[\int_{A_\infty} n_{wg}(r,\omega_i)^2 |E_i(r,\omega_i)|^2 A\right]^{\frac{1}{2}}}, \tag{6}$$

where r is the spatial coordinate in the cross-section plane, n_{wg} is the waveguide refractive index, A_0 is the waveguide cross section, A_∞ is the whole transverse plane, and $E_{j/q/l/m}$ is the mode field of each wave involved in the intermodal FWM. f_{jqlm} quantifies the coupling between the fields involved in the process. This parameter depends also on the confinement of the modes, resulting in a higher value when the modes are more confined in the waveguide core. Here it is assumed that the only significant nonlinearity is due to the waveguide core.

Not all the modal combinations are available for FWM. Equation (6) shows that only the modal combinations that give an even integrand at the numerator yield non-zero f_{jqlm}. Table 1 compares f_{jqlm} of the intermodal combination (1,2,2,1) with those of two intramodal combinations for the same waveguide geometry (3.5 μm × 243 nm) with TE polarization. The wavelengths considered are those needed for the phase-matched (1,2,2,1) TE combination, i.e., pumps at 1550 nm, signal at 1651 nm, and idler at 1461 nm.

Table 1 shows a lower relative efficiency of the intermodal FWM with respect to the intramodal FWM. The lower value, of about −3.5 dB, is mainly due to the spatial mismatch between the modes rather than to the larger effective area of the higher-order modes [see the small difference between the efficiency of the (2,2,2,2) intramodal FWM with respect to the (1,1,1,1) combination]. However, comparing the 3.5 μm × 243 nm cross section with the typical cross sections used for state–of-the-art broad wavelength conversion (0.9 μm × 220 nm, air cladding) [31], the intermodal (1,2,2,1) combination in the 3.5 μm × 243 nm waveguide exhibits −12 dB efficiency with respect to the (1,1,1,1) combination in the smaller waveguide, considering the same input power. In this case, the larger effective area of the multimode waveguide is more important than the mode fields overlap in lowering the efficiency. The efficiency improves to −8 dB with respect to the same 0.9 μm × 220 nm waveguide when considering the (1,2,2,1) combination with a 2 μm × 243 nm cross section. Despite the lower efficiency, the intermodal FWM enables larger spectral translations with respect to intramodal FWM, even when higher-order terms of the GVD are considered in intramodal FWM [31–33].

Table 1. Calculated Mode Field Overlap for a 3.5 μm × 243 nm Si Waveguide[a]

(j, q, l, m)	$\lvert f_{jqlm}^{\text{norm}} \rvert$	$\Delta\eta^{\text{norm}}$ [dB]
(1,1,1,1)	1	0
(2,2,2,2)	0.997	−0.023
(1,2,2,1)	0.666	−3.528

[a] $\lvert f_{jqlm}^{\text{norm}} \rvert$ is the mode field's overlap normalized to $\lvert f_{1111} \rvert$. $\Delta\eta^{\text{norm}}$ in dB is the difference in efficiency, at perfect phase matching, with respect to the (1,1,1,1) combination. TE polarization is considered.

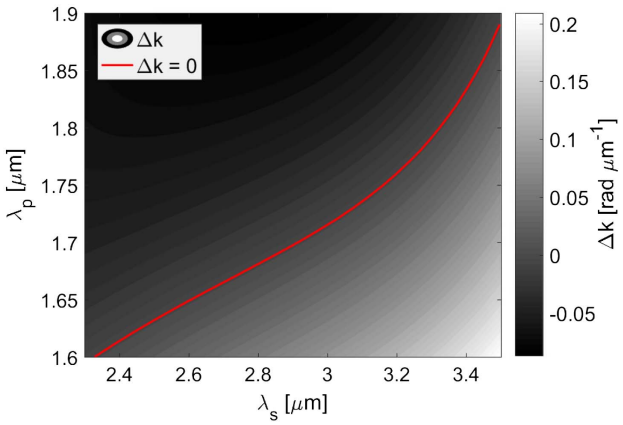

Fig. 3. Numerical simulation of Δk according to Eq. (4) for a 2-μm-wide waveguide with (1,2,2,1) intermodal combination and TE polarization. In grayscale, the Δk parameter is a function of the pump wavelength and the signal wavelength. The red line highlights the perfect phase-matching spectral position.

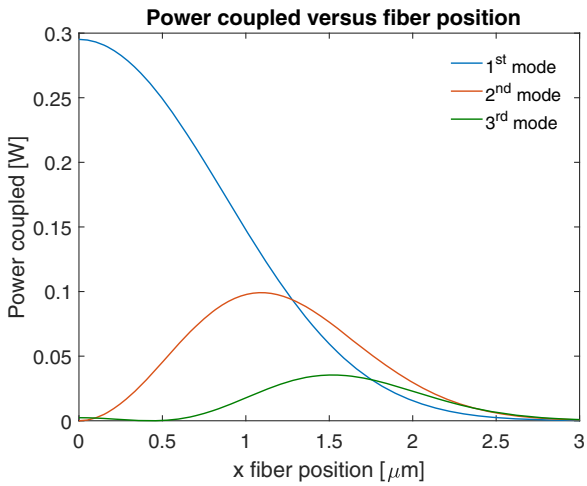

Fig. 4. Computed power coupled into the different modes of a waveguide by a tapered lensed fiber as a function of the fiber position with respect to the center of the waveguide. It is assumed a 3.5-μm-wide waveguide and 1 W at the input fiber with a wavelength of 1550 nm. When the fiber position is 0 μm, the fiber is in the middle of the waveguide. These values have been normalized with respect to the measured coupling losses for the first TE waveguide mode.

In fact, Fig. 3 shows the calculated Δk for FWM in a 2-μm-wide waveguide with the (1,2,2,1) intermodal combination and TE polarization. It is observed that, as the pump wavelength is increased, the spectral position of the phase-matching condition moves towards longer wavelengths. In this way, a very large spectral translation is obtained, with the generation of 3.5 μm signal photons when the pump approaches 1.9 μm wavelength. Clearly, at these signal wavelengths the losses related to the silica cladding start to be significant, and an air-cladding cross section is preferable in order to reduce such losses.

C. Mode Selection

The excitation of higher-order modes in a multimode silicon waveguide is achieved by properly illuminating the input facet of the waveguide. The efficiency with which the modes are excited in the waveguide is calculated through the power overlap integral ξ [34,35]

$$\xi_{x,m} = \frac{\int_{-\infty}^{\infty} dx \int_{-\infty}^{\infty} dy \psi_x E_{x,m}^* \int_{-\infty}^{\infty} dx \int_{-\infty}^{\infty} dy \psi_x^* E_{x,m}}{\int_{-\infty}^{\infty} dx \int_{-\infty}^{\infty} dy |\psi_x|^2 \int_{-\infty}^{\infty} dx \int_{-\infty}^{\infty} dy |E_{x,m}|^2}, \quad (7)$$

with the index x indicating TE polarization (y is used for TM polarization), ψ_x is the incident TE field profile, and $E_{x,m}$ is the mth TE order mode field profile. ξ quantifies how the input power is distributed among the mode supported by the waveguide. Depending on the input field profile, it is possible to excite a single waveguide mode or multiple modes [35].

In our experiment, we used a tapered lensed fiber to couple the light in the waveguide. The field profile of the tapered lensed fiber is Gaussian, with a measured waist of (1.17 ± 0.01) μm at 1550 nm. We simulated the coupling efficiency as a function of the horizontal fiber position, i.e., along the waveguide width, keeping the vertical position at half of the height of the waveguide. The fiber was assumed to be normal with respect to the waveguide facet. The power coupled in the different modes is calculated by

$$P_{p,m}^{wg} = (1 - R)\xi_{p,m} P_p, \quad (8)$$

where m is the order mode, $p = x, y$ refers to the polarization, R is the facet reflection coefficient, and P_p is the input power. In Fig. 4 the computed power coupled in the first three waveguide modes is shown, considering 1 W power in the input fiber and a waveguide width of 3.5 μm. Figure 4 shows that higher-order modes can be excited by moving the input fiber along the waveguide width, with 0 μm corresponding to the center of the waveguide. The same coupling method was used also for the output signal collection.

3. EXPERIMENT

A. Setup

We used the same setup for the measurement of both the sFWM and the SFWM, shown in Fig. 5. The only difference is that in the spontaneous case no seed signal is required. A pulsed pump beam with 1550 nm wavelength, 40 ps pulse duration, and 10 MHz repetition rate is mixed through a free-space beam splitter with the continuous wave (CW) seed signal, whose wavelength can be tuned in the range 1480–1670 nm. On both the beams a polarization controller stage is present. The two beams are then coupled in a tapered lensed fiber through a collimator. To excite the proper waveguide mode, the input fiber is moved along the x axis with a piezocontrolled translator stage. The SOI chip used has several multimode waveguides with different waveguide widths. An infrared camera coupled to a microscope allows controlling the selected waveguide. The light transmitted by the waveguide is then collected at the output by another tapered lensed fiber mounted on a piezocontrolled translator stage. Then, the signals are analyzed by a monochromator when their optical power is lower than 0.1 nW or by an optical spectrum analyzer (OSA) for larger powers. The monochromator was homemade, using a grating in a double-pass configuration. The monochromator

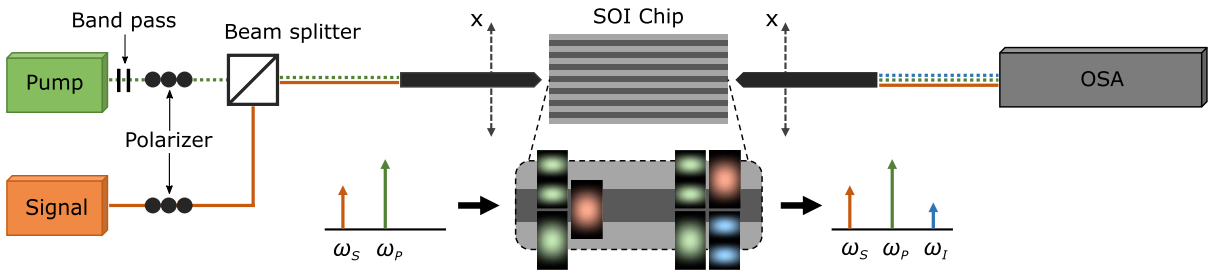

Fig. 5. Setup for the sFWM. The pump is initially filtered with two 1550 nm bandpass filters. Then, the pump and the signal, after a polarization controller stage, are mixed by a free-space beam splitter and coupled in the same tapered lensed fiber through a collimator. The input fiber injects the light in the desired waveguide on the SOI chip. The light is collected from the waveguide by another tapered lensed fiber. The position of both fibers is controlled by means of two *XYZ* nanopositioning stages via piezocontrollers. The collected light is analyzed with an OSA or a monochromator, depending on the power of the generated signal. In the inset, the waveguide modes involved in the intermodal FWM are sketched by showing the mode profiles at the input and at the output of the waveguide; as an example, the case of the (1,2,2,1) modal combination is considered. For the SFWM, the setup is exactly the same, except for the lack of the input signal.

is coupled to an InGaAs single-photon counter, allowing for a dynamic range of 10^5, i.e., from 1 fW to 0.1 nW. This large dynamic range is possible thanks to a gated measurement with the pump laser trigger. Note that the use of the InGaAs photodetector limits our measurements to the wavelength region 1200–1700 nm.

We characterized a 3.5-μm-wide waveguide, measuring the propagation losses (4.6 dB · cm^{-1}) and the coupling losses (–5.3 dB) for the first TE order mode at a wavelength of 1550 nm. The coupling losses for the second TE order mode (–10.0 dB) are estimated from the simulation (Fig. 4). The coupling losses are evaluated considering the position of the fiber that maximizes the coupling of the considered order mode (first mode—$x = 0$ μm, second mode—$x = 1.1$ μm). Finally, in our simulations, we assumed for the second-order mode the same propagation losses as for the first one, which is an optimistic assumption.

B. Coupled Wave Equations of FWM

We simulated the process by numerically solving the coupled wave equations of FWM [9]. Since the dispersion length $L_D = T_0^2/\beta_2$ [36], with T_0 the pulse duration and β_2 the GVD, is much longer than the waveguide length (e.g., $L_D = 1$ km for the first TE mode in a 2-μm-wide waveguide at $\lambda = 1550$ nm), we neglected the temporal dependence, and we considered CWs in the coupled equations, where for the power the peak power of the pulses is used. The dependence on frequency and position of the wave amplitude u is omitted for reasons of compactness.

The coupled amplitude wave equations that we used describe FWM, SPM, and cross-phase modulation, considering also the presence of free carriers (FCs). The coupled equations used are here reported

$$\frac{du_1}{dz} = -\frac{\alpha_1}{2}u_1 - \frac{F_1}{2}u_1 + i[\gamma_1|u_1|^2 + 2(\gamma_{12}|u_2|^2 + \gamma_{1s}|u_s|^2 + \gamma_{1i}|u_i|^2)]u_1 + 2i\gamma_{1is2}\sqrt{\frac{P_2P_iP_s}{P_1}}u_iu_su_2^*e^{i\Delta k_L z}, \tag{9a}$$

$$\frac{du_2}{dz} = -\frac{\alpha_2}{2}u_2 - \frac{F_2}{2}u_2 + i[\gamma_2|u_2|^2 + 2(\gamma_{21}|u_1|^2 + \gamma_{2s}|u_s|^2 + \gamma_{2i}|u_i|^2)]u_2 + 2i\gamma_{2is1}\sqrt{\frac{P_1P_iP_s}{P_2}}u_iu_su_1^*e^{i\Delta k_L z}, \tag{9b}$$

$$\frac{du_i}{dz} = -\frac{\alpha_i}{2}u_i - \frac{F_i}{2}u_i + i[\gamma_i|u_i|^2 + 2(\gamma_{i1}|u_1|^2 + \gamma_{i2}|u_2|^2 + \gamma_{is}|u_s|^2)]u_i + 2i\gamma_{i12s}\sqrt{\frac{P_1P_2P_s}{P_i}}u_1u_2u_s^*e^{-i\Delta k_L z}, \tag{9c}$$

$$\frac{du_s}{dz} = -\frac{\alpha_s}{2}u_s - \frac{F_s}{2}u_s + i[\gamma_s|u_s|^2 + 2(\gamma_{s1}|u_1|^2 + \gamma_{s2}|u_2|^2 + \gamma_{si}|u_i|^2)]u_s + 2i\gamma_{s12i}\sqrt{\frac{P_1P_2P_i}{P_s}}u_1u_2u_i^*e^{-i\Delta k_L z}, \tag{9d}$$

where $\hat{\boldsymbol{z}}$ is the propagation direction; the labels $\nu = 1, 2, s, i$ refer to the first pump photon, the second pump photon, the signal, and the idler, respectively; α_ν is the attenuation coefficient; and P_ν is the power. Regarding the FCs

$$F_\nu = \sigma_\nu(1 + i\mu_\nu)N, \tag{10}$$

where N is the free-carrier density generated by the pumps, evaluated through the rate equation with 30 ns FCs lifetime [37], and

$$\sigma_\nu = \frac{1}{N}\frac{c\kappa_\nu}{n(\omega_\nu)v_{g,\nu}}\delta_{\alpha_{FC}}, \qquad \mu_\nu = -\frac{1}{\sigma_\nu N}\frac{2\omega_\nu\kappa_\nu}{n(\omega_\nu)v_{g,\nu}}\delta_{n_{FC}}, \tag{11}$$

with n the bulk Si refractive index, ω_ν the frequency, $v_{g,\nu}$ the group velocity, $\delta_{\alpha_{FC}}$ the free-carrier absorption (FCA) coefficient, $\delta_{n_{FC}}$ the free-carrier dispersion (FCD) coefficient, and

$$\kappa_\nu = \frac{n(\omega_\nu)^2 \int_{A_0} |E_\nu(r,\omega_\nu)|^2 \mathrm{d}A}{\int_{A_\infty} n_{wg}(r,\omega_\nu)^2 |E_\nu(r,\omega_\nu)|^2 \mathrm{d}A}. \quad (12)$$

Consider that in the case of nonlinear optical processes the FCs are mainly generated through two-photon absorption (TPA), with the same density of electrons and holes; because of this, we calculated the coefficients $\delta_{\alpha_{FC}}$ and $\delta_{n_{FC}}$ as [9]

$$\delta_{\alpha_{FC}} = 14.5 \times 10^{-18} N, \quad (13)$$

$$\delta_{n_{FC}} = -8.8 \times 10^{-22} N - 8.5 \times 10^{-18} N^{0.8}. \quad (14)$$

Regarding the γ coefficients, with the labels a, b, c, d referring to $1, 2, s, i$,

$$\gamma_{adcd} = \frac{3\omega_a \sqrt{n_{g,a} n_{g,b} n_{g,c} n_{g,d}}}{4\varepsilon_0 A_0 c^2} \Gamma_{abcd}, \quad (15)$$

with $n_{g,\nu}$ the group index, ε_0 the vacuum permittivity, and

$$\Gamma_{abcd} = A_0 \frac{\int_{A_0} E_a^*(r,\omega_a) \chi^{(3)} \vdots E_b(r,\omega_b) E_c^*(r,\omega_c) E_d(r,\omega_d)\, \mathrm{d}A}{\prod_{\nu=abcd} \left[\int_{A_\infty} n_{wg}(r,\omega_\nu)^2 |E_\nu(r,\omega_\nu)|^2 \mathrm{d}A \right]^{1/2}}, \quad (16)$$

where $\chi^{(3)}$ is the third-order susceptibility. The other γ are defined as $\gamma_{ab} = \gamma_{abba}$ and $\gamma_a = \gamma_{aaaa}$. In Eq. (9), the higher-order modes are taken into account by using their field profiles and effective index dispersions. We assumed the same attenuation coefficient for all the waves. For further details regarding Eq. (9), see Ref. [9].

C. Measurements and Results

We investigated several modal combinations for the intermodal FWM: (1,2,2,1)-TE, (1,2,2,1)-TM, (1,1,2,2)-TE, (1,3,3,1)-TE, and (1,3,3,1)-TM. Here we focus mainly on the (1,2,2,1)-TE modal combination. We performed the measurements on 15 different waveguides with the same nominal width of 3.5 μm and 1.5 cm length. We measured an average idler wavelength $\bar{\lambda}_I = 1467.6$ nm with standard deviation $\sigma = 3.5$ nm. This finding is in agreement with the numerical computed idler peak wavelength of 1467 nm. The deviation from the computed value is mainly due to fabrication imperfections, which led to waveguide width different from the nominal one. In Fig. 6(a) the spectrum of the SFWM for one of the 3.5-μm-wide waveguides is reported. In this particular case, we measured $\lambda_I = 1469$ nm and $\lambda_S = 1640$ nm. The measurement was performed with the input fiber at $x = 0.83$ μm, a position that maximizes the product between the coupled power on the first- and second-order modes. The input on-chip peak pump power is about 3.1 W (2.1 W on the first-order mode and 1.0 W on the second one). For this measurement, the fiber-to-fiber losses are 17.9 dB or 22.6 dB, coupling at the output the first or the second TE mode, respectively. For this calculation, we are considering the input fiber fixed at 0.83 μm, with −5.7 dB total coupling losses for the pump.

To confirm the FWM origin of these peaks, we measured the pump power dependence of their intensity. In Fig. 7, the average on-chip generation rate is reported as a function of the on-chip average pump power. The expected quadratic dependence is measured for pump powers $P_P < 0.5$ mW, see the inset in Fig. 7, while for higher powers the efficiency of the process decreases due to TPA, which depletes the pump power. We estimate an average generation rate of $24.6 \pm 0.8 (\frac{\mathrm{MHz}}{\mathrm{mW}^2}) P_P^2$ for the 3.5-μm-wide waveguide in the pump power range 0–0.5 mW. This measurement was performed by monitoring the idler photon counts.

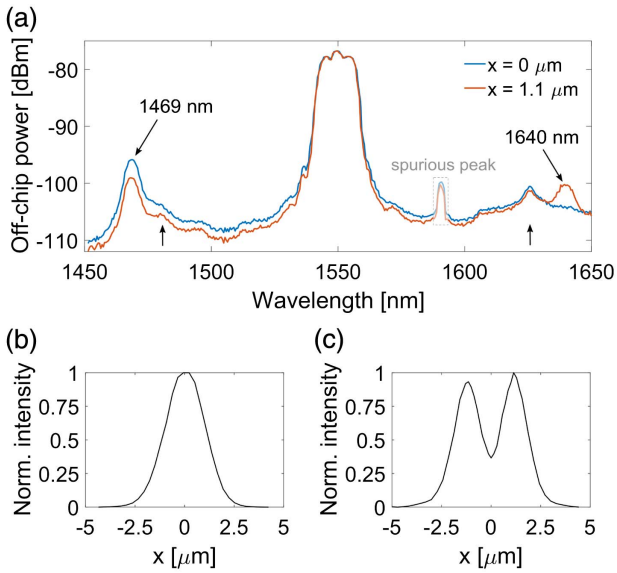

Fig. 6. (a) Spectra of the SFWM in a 3.5-μm-wide waveguide, with the (1,2,2,1) combination and TE polarization. The pump is at 1550 nm. The different lines refer to the different positions of the output fiber: the blue line refers to the spectrum measured with the output fiber in the middle of the waveguide, and the red line refers to the spectrum measured with the output fiber at 1.1 μm with respect to the center of the waveguide. The two vertical arrows indicate a spurious signal due to Raman scattering occurring in the input fiber. (b) Intensity profile at the output facet of the waveguide, for the peak at 1469 nm in (a). (c) Intensity profile at the output facet of the waveguide, for the peak at 1640 nm in (a).

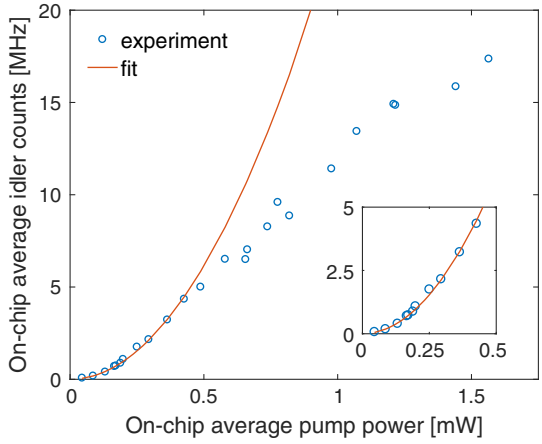

Fig. 7. Average on-chip photon generation rate for the SFWM process as a function of the on-chip average pump power. The blue circles are the experimental measurements, while the red line is the quadratic fit of the data belonging to the 0–0.5 mW range. The inset shows the low pump power region.

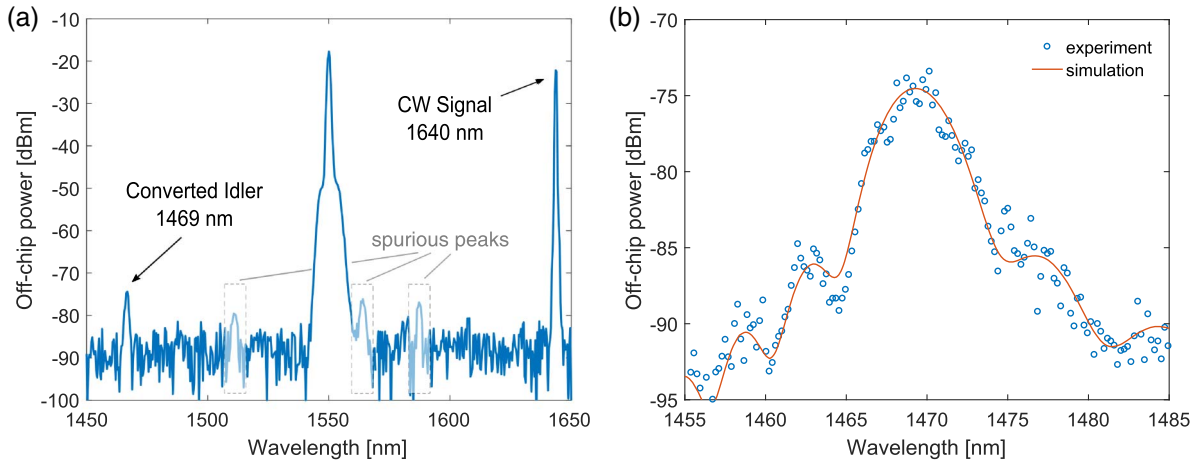

Fig. 8. (a) Spectrum of the sFWM with the (1,2,2,1) TE intermodal combination in a 3.5-μm-wide waveguide. The stimulating CW signal at 1640 nm is converted into the pulsed idler at 1469 nm. The smaller peaks are spurious signals due to the OSA. (b) Spectrum of the stimulated idler generation efficiency with the intermodal FWM combination (1,2,2,1) TE in a 3.5-μm-wide waveguide. The simulation was performed with a 3.66-μm-wide waveguide. The blue circles are the measured data, while the orange line is the simulation. This measurement was performed by synchronously scanning the signal wavelength and the monochromator wavelength in order to read the idler power corresponding to the input signal. The simulated spectrum was shifted by −3.3 dBm in order to match the experimental data.

We verified the intermodal nature of the process by measuring the spectrum with two different horizontal positions of the output fiber. In fact, since the idler is generated on the first-order mode and the signal on the second-order mode, according to Fig. 4, we expect to observe the maximum intensity for the idler when the output fiber position is $x = 0$ μm, i.e., in the middle of the waveguide, and the maximum intensity for the signal when the position of the output fiber is at 1.1 μm, i.e., when the coupling of the second-order mode is maximized. In Fig. 6(a), the spectrum measured with the output fiber at $x = 0$ μm exhibits only one peak at 1469 nm, the idler peak. In fact, from simulation in Fig. 4, we expect, at $x = 0$ μm, a negligible coupling efficiency for the second-order mode. When the output fiber is placed at 1.1 μm, also the signal peak appears at 1640 nm, as expected.

Another evidence of the intermodal nature of the SFWM is the spatial profile of the generated idler and signal waves on the output waveguide facet. To do this measurement, we set the monochromator to resolve either the signal or the idler peak wavelengths, and then we performed an intensity profile scan on the output facet of the waveguide along the x axis (see Fig. 5). In Figs. 6(b) and 6(c), we report the measured profiles for the idler and signal, respectively, which exhibit the expected one-lobe (first-order) and the two-lobe (second-order) shapes.

The stimulated FWM was measured in the same 3.5-μm-waveguide with 1.5 cm length. An example of the measured spectrum is shown in Fig. 8(a). For this measurement, the on-chip input peak pump power was about 1 W (0.7 W on the first mode and 0.3 W on the second) at 1550 nm, and the input on-chip signal power was about 47 μW at 1640 nm on the second-order mode. An idler peak at 1469 nm is generated with −14.7 dB maximum conversion efficiency [38], calculated as the ratio between the on-chip idler peak power and the on-chip signal power, evaluated at the end of the waveguide. The input on-chip powers are estimated from the off-chip power reported in Fig. 8(a) and considering the propagation and coupling losses. Regarding the coupling losses, the measurement reported in Fig. 8(a) was performed with the input fiber at $x = 0.83$ μm and the output fiber at $x = 0$ μm.

By synchronously scanning the signal wavelength and the monochromator wavelength according to the energy conservation equation, it is possible to measure the spectrum of the sFWM. We considered again the stimulated intermodal FWM with the (1,2,2,1) combination in the 3.5-μm-wide waveguide.

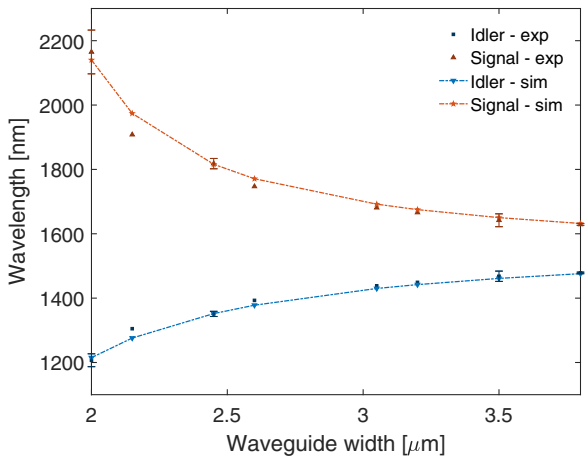

Fig. 9. Phase-matched wavelengths as a function of the waveguide width for the (1,2,2,1) combination, TE polarization, and 1550 nm pump. The experimental idler and signal are reported in blue and red, respectively, while the corresponding simulated values are reported by the light blue and orange points, where the lines are a guide for the eye. The phase-matched signal wavelengths have been deduced by using Eq. (1) and the measured idler wavelengths. For some widths (those with the error bars), we performed repeated measurements (ten measurements) on nominally identical waveguides. The theory and the experiment are in agreement.

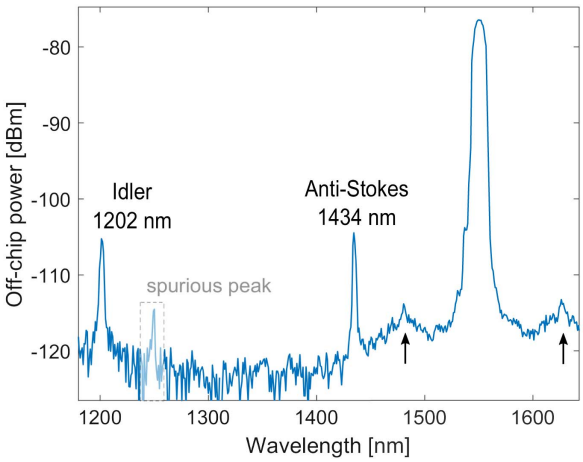

Fig. 10. Spectrum of the SFWM for the (1,2,2,1) combination, TE polarization, and a 2-μm-wide waveguide. The pump is at 1550 nm with an on-chip peak power of about 3.9 W (3.3 W on the first-order mode, 0.6 W on the second one). The idler is generated at 1202 nm. The peak at 1434 nm is the anti-Stokes peak of the Si Raman scattering. The two vertical arrows indicate the spurious signals due to Raman scattering occurring in the input fiber.

Figure 8(b) compares the measured and simulated spectra of the stimulated idler. A good agreement is observed. The simulation considered a width of 3.66 μm for the waveguide in order to match the peak wavelength. This could be due to a difference of 0.16 μm with respect to the nominal 3.5 μm width. The measured 3 dB bandwidth is 4.7 ± 0.2 nm, compatible with the simulated 4.8 nm 3 dB bandwidth.

According to Eq. (4), it is possible to tune the phase-matching position by controlling the effective index of the modes involved in the intermodal FWM, i.e., by changing the waveguide cross section. Therefore, we measured the intermodal SFWM with the (1,2,2,1) modal combination and TE polarization in several waveguides, with widths ranging from 2 to 3.8 μm. Due to the use of the InGaAs detector, we could only trace the evolution of the idler spectral position while we computed the corresponding spectral position of the signal imposing the energy conservation. As the waveguide width is increased, the spectral distance between the signal and idler reduces, as shown in Fig. 9. Figure 9 shows that the waveguide geometry and the spectral translation $\Delta\lambda = \lambda_S - \lambda_I$ are tightly correlated, which allows an easy tunability of the phase-matched wavelengths. Moreover, the intermodal phase-matching approach allows for extremely large spectral translation in a narrow waveguide. An example is shown in Fig. 10, where the SFWM spectrum for a 2-μm-wide waveguide pumped at 1550 nm is shown. The generated idler is at 1202 nm, and the expected signal is at 2181.6 nm, resulting in 979.6 nm spectral distance between signal and idler. This is the largest detuning ever reported for FWM on a silicon chip with a C-band pump source. Note that in Fig. 10, it is also possible to see the anti-Stokes Raman peak at 1434 nm, which can be used as a reference for the efficiency of the process.

We also investigated other modal combinations. We performed the SFWM measurements in a waveguide with a nominal width of 3.8 μm, with 1.5 cm length, observing peaks corresponding to the modal combinations reported in Fig. 11. Three spectra are shown, two for the TE combinations and one for the TM combinations. The TE measurements were performed with an on-chip peak power of about 16.1 W on the first mode, 0.2 W on the second mode, and 0.4 W on the third mode. The on-chip peak power for the TM case was about 10.4 W on the first mode, 5.2 W on the second mode, and 0.4 W on the third mode. The TE combinations required two spectra, one with the output fiber at $x = 0$ μm and one at $x = 1.25$ μm, in order to enlighten the different modes involved in the combinations (1,3,3,1) and (1,1,2,2). In fact, the idler on the first-order mode is better coupled when $x = 0$ μm, while the idler of the second-order mode is when $x = 1.25$ μm. Table 2 compares the measured and simulated

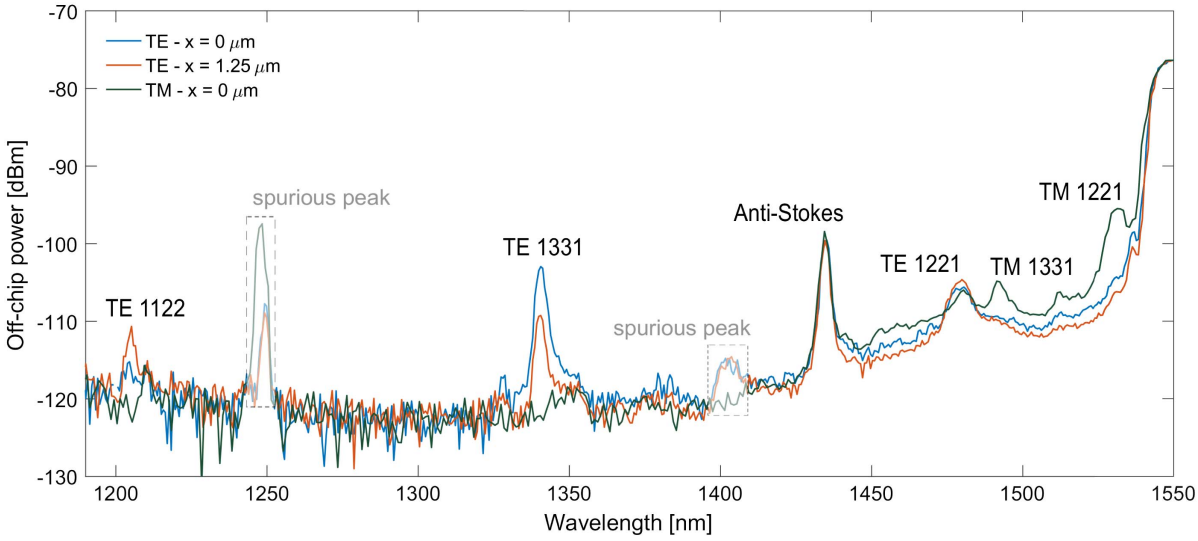

Fig. 11. Spectra of intermodal SFWM in a 3.8-μm-wide waveguide. Both TE and TM measurements are reported. The position of the output fiber is reported in the legend. The peaks refer to the indicated combinations. The pump is at 1550 nm.

Table 2. Intermodal Combinations Measured in Fig. 11[a]

(j,q,l,m)	Polarization	λ_I^{sim} [nm]	λ_I^{exp} [nm]
(1,1,2,2)	TE	1211	1205
(1,2,2,1)	TE	1479	1479
(1,3,3,1)	TE	1346	1340
(1,2,2,1)	TM	1525	1531
(1,3,3,1)	TM	1480	1492

[a] λ_I^{sim} and λ_I^{exp} are the simulated and the measured idler wavelengths. The simulation is performed with a 3.84-μm-wide waveguide.

idler wavelengths for the combinations shown in Fig. 11. A good agreement is observed.

4. CONCLUSIONS

In this work we demonstrate on-chip intermodal FWM. By measuring both spontaneous and stimulated FWM via intermodal phase-matching in SOI waveguides, we proved a new on-chip approach to large spectral translation. The intermodal approach allows for broadband and tunable phase matching, which we exploited to achieve spontaneous generation of 1202 nm light in a 2-μm-wide waveguide, with 979.6 nm spectral distance with respect to the twin signal photons or with 348 nm spectral distance with respect to the 1550 nm pump photons. Moreover, since the phase matching with higher-order modes does not rely on the fourth-order dispersion coefficient β_4 of the GVD, the phase-matched wavelengths are less affected by fabrication imperfections with respect to discrete band phase matching based on the compensation of the higher-order GVD terms. The multimode waveguides are larger than common single-mode waveguides, with lower losses and less issues in terms of relative deviations from the nominal waveguide dimensions. Involving higher-order modes in the FWM process clearly negatively affects the efficiency of the process, which reduces with the decreased mode field overlap. Despite this lower efficiency with respect to common intramodal FWM, the intermodal approach enables larger spectral translations and opens new functionalities for technologies involving higher-order modes. Moreover, we measured several modal combinations, demonstrating the flexibility of the intermodal FWM, whose application is not limited at the first two order modes.

Nonetheless, intermodal FWM can provide a suitable mechanism for the creation of heralded single-photon sources where the large spectral distance between the involved photons allows an easy filtering of the pump photons and the use of optimized single-photon detectors. The approach here proposed has been demonstrated by using silicon photonics; however, it can be easily extended to other classes of materials. Specifically, the use of other materials is relevant to overcome the detrimental effect of TPA, which is particularly large in Si waveguides.

Funding. Provincia Autonoma di Trento supported this research by the (SiQuro) project within the Grandi progetti 2012 call; Ministero dell'Istruzione, dell'Università e della Ricerca (MIUR) with the PRIN project NEMO (2015KEZNYM).

Acknowledgment. S. Signorini thanks Dr. Fernando Ramiro Manzano for support with the monochromator system. M. Ghulinyan and G. Pucker thank the MNFLab-FBK staff for support in realizing the samples.

REFERENCES AND NOTES

1. D. Dai and J. E. Bowers, "Silicon-based on-chip multiplexing technologies and devices for peta-bit optical interconnects," Nanophotonics **3**, 283–311 (2014).
2. S. Berdagu and P. Facq, "Mode division multiplexing in optical fibers," Appl. Opt. **21**, 1950–1955 (1982).
3. S. Bagheri and W. M. Green, "Silicon-on-insulator mode-selective add-drop unit for on-chip mode-division multiplexing," in *Proceedings of IEEE Conference on Group IV Photonics* (IEEE, 2009).
4. L. W. Luo, N. Ophir, C. P. Chen, L. Gabrielli, C. B. Poitras, K. Bergmen, and M. Lipson, "WDM-compatible mode-division multiplexing on a silicon chip," Nat. Commun. **5**, 3069 (2014).
5. Y. Ding, J. Xu, H. Ou, and C. Peuchere, "Mode-selective wavelength conversion based on four-wave mixing in a multimode silicon waveguide," Opt. Express **22**, 127–135 (2014).
6. M. Ma and L. Chen, "On-chip silicon mode-selective broadband wavelength conversion based on cross-phase modulation," in *Conference on Lasers and Electro-Optics*, OSA Technical Digest (Optical Society of America, 2016), paper STh3E.3.
7. Y. Qiu, X. Li, M. Luo, D. Chen, J. Wang, J. Xu, Q. Yang, and S. Yu, "Mode-selective wavelength conversion of OFDM-QPSK signals in a multimode silicon waveguide," Opt. Express **25**, 4493–4499 (2017).
8. R. W. Boyd, *Nonlinear Optics* (Academic, 2003).
9. M. Borghi, C. Castellan, S. Signorini, A. Trenti, and L. Pavesi, "Nonlinear silicon photonics," J. Opt. **19**, 093002 (2017).
10. M. A. Foster, A. C. Turner, J. E. Sharping, B. S. Schmidt, M. Lipson, and A. L. Gaeta, "Broad-band optical parametric gain on a silicon photonic chip," Nature **441**, 960–963 (2006).
11. K. Guo, L. Lin, J. Christensen, E. Christensen, X. Shi, Y. Ding, K. Rottwitt, and H. Ou, "Broadband wavelength conversion in a silicon vertical-dual-slot waveguide," Opt. Express **25**, 32964–32971 (2017).
12. R. J. Essiambre, M. A. Mestre, R. Ryf, A. H. Gnauck, R. W. Tkach, A. R. Chraplyvy, Y. Sun, X. Jiang, and R. Lingle, "Experimental investigation of inter-modal four-wave mixing in few-mode fibers," IEEE Photon. Technol. Lett. **25**, 539–542 (2013).
13. H. Pourbeyram, E. Nazemosadat, and A. Mafi, "Detailed investigation of intermodal four-wave mixing in SMF-28: blue-red generation from green," Opt. Express **23**, 14487–14500 (2015).
14. W. Pan, Q. Jin, X. Li, and S. Gao, "All-optical wavelength conversion for mode-division multiplexing signals using four-wave mixing in a dual-mode fiber," J. Opt. Soc. Am. B **32**, 2417–2424 (2015).
15. S. Friis, I. Begleris, Y. Jung, K. Rottwitt, P. Petropoulos, D. Richardson, P. Horak, and F. Parmigiani, "Inter-modal four-wave mixing study in a two-mode fiber," Opt. Express **24**, 30338–30349 (2016).
16. J. Yuan, Z. Kang, F. Li, X. Zhang, X. Sang, G. Zhou, Q. Wu, B. Yan, K. Wang, C. Yu, H. Tam, and P. Wai, "Demonstration of intermodal four-wave mixing by femtosecond pulses centered at 1550 nm in an air-silica photonic crystal fiber," J. Lightwave Technol. **35**, 2385–2390 (2017).
17. R. Dupiol, A. Bendahmane, K. Krupa, J. Fatome, A. Tonello, M. Fabert, V. Couderc, S. Wabnitz, and G. Millot, "Intermodal modulational instability in graded-index multimode optical fibers," Opt. Lett. **42**, 3419–3422 (2017).
18. F. Parmigiani, Y. Jung, S. M. M. Friis, Q. Kang, I. Begleris, P. Horak, K. Rottwitt, P. Petropoulos, and D. J. Richardson, "Study of inter-modal four wave mixing in two few-mode fibres with different phase matching properties," in *Proceedings of 42nd European Conference on Optical Communication* (2016).
19. R. H. Stolen, J. E. Bjorkholm, and A. Ashkin, "Phase-matched three-wave mixing in silica fiber optical waveguides," Appl. Phys. Lett. **24**, 308–310 (1974).

20. J. Cheng, M. E. Pedersen, K. Charan, K. Wang, C. Xu, L. Grner-Nielsen, and D. Jakobsen, "Intermodal four-wave mixing in a higher-order-mode fiber," Appl. Phys. Lett. **101**, 161106 (2012).
21. H. Tu, Z. Jiang, D. L. Marks, and S. A. Boppart, "Intermodal four-wave mixing from femtosecond pulse-pumped photonic crystal fiber," Appl. Phys. Lett. **94**, 101109 (2009).
22. S. Signorini, M. Mancinelli, M. Bernard, M. Ghulinyan, G. Pucker, and L. Pavesi, "Broad wavelength generation and conversion with multi modal four wave mixing in silicon waveguides," in *Proceedings of IEEE Conference on Group IV Photonics* (IEEE, 2017), pp. 59–60.
23. E. A. Kittlaus, N. T. Otterstrom, and P. T. Rakich, "On-chip inter-modal Brillouin scattering," Nat. Commun. **8**, 15819 (2017).
24. J. G. Crowder, S. D. Smith, A. Vass, and J. Keddie, "Infrared methods for gas detection," in *Mid-Infrared Semiconductor Optoelectronics* (Springer, 2006), pp. 595–613.
25. M. Mancinelli, A. Trenti, S. Piccione, G. Fontana, J. S. Dam, P. Tidemand-Lichtenberg, C. Pedersen, and L. Pavesi, "Mid-infrared coincidence measurements on twin photons at room temperature," Nat. Commun. **8**, 15184 (2017).
26. B. Kuyken, P. Verheyen, P. Tannouri, X. Liu, J. Van Campenhout, R. Baets, W. Green, and G. Roelkens, "Generation of 3.6 μm radiation and telecom-band amplification by four-wave mixing in a silicon waveguide with normal group velocity dispersion," Opt. Lett. **39**, 1349–1352 (2014).
27. S. K. Liao, H. L. Yong, C. Liu, G. L. Shentu, D. D. Li, J. Lin, H. Dai, S. Q. Zhao, B. Li, J. Y. Guan, W. Chen, Y. H. Gong, Y. Li, Z. H. Lin, G. S. Pan, J. S. Pelc, M. M. Fejer, W. Z. Zhang, W. Y. Liu, J. Yin, J. G. Ren, X. B. Wang, Q. Zhang, C. Z. Peng, and J. W. Pan, "Long-distance free-space quantum key distribution in daylight towards inter-satellite communication," Nat. Photonics **11**, 509–513 (2017).
28. A. C. Turner, C. Manolatou, B. S. Schmidt, M. Lipson, M. A. Foster, J. E. Sharping, and A. L. Gaeta, "Tailored anomalous group-velocity dispersion in silicon channel waveguides," Opt. Express **14**, 4357–4362 (2006).
29. C. Lin and M. A. Bsch, "Large-Stokes-shift stimulated four-photon mixing in optical fibers," Appl. Phys. Lett. **38**, 479–481 (1981).
30. Y. Xiao, R. J. Essiambre, M. Desgroseilliers, A. M. Tulino, R. Ryf, S. Mumtaz, and G. P. Agrawal, "Theory of intermodal four-wave mixing with random linear mode coupling in few-mode fibers," Opt. Express **22**, 32039–32059 (2014).
31. X. Liu, B. Kuyken, G. Roelkens, R. Baets, R. M. Osgood, Jr., and W. M. Green, "Bridging the mid-infrared-to-telecom gap with silicon nanophotonic spectral translation," Nat. Photonics **6**, 667–671 (2012).
32. Q. Lin, J. Zhang, P. M. Fauchet, and G. P. Agrawal, "Ultrabroadband parametric generation and wavelength conversion in silicon waveguides," Opt. Express **14**, 4786–4799 (2006).
33. M. A. Foster, A. C. Turner, R. Salem, M. Lipson, and A. L. Gaeta, "Broad-band continuous-wave parametric wavelength conversion in silicon nanowaveguides," Opt. Express **15**, 12949–12958 (2007).
34. W. S. Chang, *Fundamentals of Guided-Wave Optoelectronic Devices* (Cambridge University, 2009).
35. S. Signorini, M. Borghi, M. Mancinelli, M. Bernard, M. Ghulinyan, G. Pucker, and L. Pavesi, "Oblique beams interference for mode selection in multimode silicon waveguides," J. Appl. Phys. **122**, 113106 (2017).
36. G. P. Agrawal, *Nonlinear Fiber Optics* (Academic, 2013).
37. R. M. Osgood, N. C. Panoiu, J. I. Dadap, X. Liu, X. Chen, I.-W. Hsieh, E. Dulkeith, W. M. J. Green, and Y. A. Vlasov, "Engineering nonlinearities in nanoscale optical systems: physics and applications in dispersion-engineered silicon nanophotonic wires," Adv. Opt. Photon. **1**, 162–235 (2009).
38. The conversion efficiency is calculated as the ratio between the on-chip idler peak power and the on-chip signal power, both evaluated at the end of the waveguide. The input on-chip signal power was about 47 μW (= −13.3 dB) at 1640 nm on the second-order mode. At the end of the waveguide, considering 4.6 $dB \cdot cm^{-1}$ of propagation losses and 1.5 cm waveguide length, the signal power on the second-order mode is −20.2 dBm. The off-chip generated average idler power is about −74.2 dBm, as shown in Fig. 8(a). Considering the coupling losses for the first-order mode, 5.3 dB, the on-chip average idler power is −68.9 dBm. Considering that the pump laser has 10 MHz repetition rate and 40 ps pulse width, the on-chip idler peak power, at the end of the waveguide, is −34.9 dBm. Therefore, the conversion between the signal power, −20.2 dBm, and the idler peak power, −34.9 dBm, is −14.7 dB.